Analyst

ROYAL SOCIETY OF CHEMISTRY

PAPER

View Article Online
View Journal | View Issue

Cite this: *Analyst*, 2022, **147**, 4141

Characterisation of Sr^{2+} mobility in osteoporotic rat bone marrow by cryo-ToF-SIMS and cryo-OrbiSIMS†

Christine Kern, [a] Reem Jamous,[b] Thaqif El Khassawna[b] and Marcus Rohnke *[a]

Strontium (Sr^{2+}) ions are an effective therapeutic agent for the healing of osteoporotic bone fractures and are therefore used, for example, in form of strontium-modified bone cements. In order to reduce animal testing in further implant materials development in the future, a simulation of the Sr^{2+} release and transport in bone would be helpful. For such a simulation, knowledge of the experimental parameters for Sr^{2+} mobility in different compartments of bone (mineralised bone, bone marrow) is essential. In a previous study, we developed an experimental protocol for transport studies in bovine bone marrow by time-of-flight secondary ion mass spectrometry (ToF-SIMS). In the current proof-of-concept study, we investigated Sr^{2+} diffusion for the first time in bone marrow of rat bone sections. Additionally, orbitrap secondary ion mass spectrometry (OrbiSIMS) was applied for unambiguous signal identification of lipids and fatty acid species in rat bone marrow. Detailed 2D and 3D mass spectrometric imaging analyses, depth profiling as well as OrbiSIMS spectrometric analysis revealed faster Sr^{2+} diffusion in rat bone marrow areas with low intensity of lipid and fatty acid signals than in areas with higher lipid/fatty acid content. These results could be confirmed by histological staining and additional analysis of Sr^{2+} diffusion into pure fat sections.

Received 1st June 2022,
Accepted 28th July 2022

DOI: 10.1039/d2an00913g

rsc.li/analyst

1. Introduction

Osteoporosis is an age-related disease, characterised by a decrease in bone density due to loss of bone mineral content, and changes of bone microstructure.[1,2] These alterations of the bone structure result in an instability of osteoporotic bone that can lead to more frequent fractures and subsequently to delayed or incomplete fracture healing.[1] In order to meet the special challenges of osteoporotic bone fracture healing, when researching new implant materials, not only fracture stabilisation plays an important role. Rather, next generation implants must also take into account the specific needs, biomechanics, and impaired remodeling capabilities of systemically altered bone. Therefore, these implant materials should actively contribute to accelerated and improved regeneration of the damaged bone, *e.g.*, through the release of therapeutic agents or drugs.

Over the years, strontium in form of Sr^{2+} ions has emerged as one of these effective substances for use in osteoporosis treatment. Specifically, Sr^{2+} is capable of both stimulating new bone formation and reducing bone resorption, thus having an overall positive effect on bone healing[3–7] which can contribute to a rebalanced bone remodelling.[4,7–13] For example, Sr^{2+}-containing calcium phosphate cements displayed positive effects on bone cells[10,14,15] and fracture healing process of osteoporotic bone, both *in vitro* and *in vivo*.[4,8,9,16] Moreover, local release of Sr^{2+} ions from strontium-functionalised titanium implant surfaces improved both implant fixation and osseointegration of the implant.[12,17–19]

For further development, evaluation, and optimisation of new functionalised biomaterials for systemically altered, osteoporotic bone, knowledge of the distribution of healing-promoting agents such as Sr^{2+} in bone is essential. Mathematical modelling of the dispersion behaviour of Sr^{2+} could reduce the need for animal testing in the development of new biomaterials in future. In order to be able to perform such a simulation, it is necessary to determine the transport kinetics of Sr^{2+} in different bone compartments. In previous studies, we successfully applied ToF-SIMS depth profiling to determine the diffusion coefficients of Sr^{2+} in the mineralised parts of bone, namely in trabecular rat bone[20] as well as in cortical rat bone.[21] ToF-SIMS, a mass spectrometric imaging technique, enables the simultaneous detection of both organic and inorganic substances within the same sample in one analysis process in 2D and 3D. Due to the high sensitivity and high-resolution imaging capability of ToF-SIMS with a lateral resolu-

[a]*Institute of Physical Chemistry, Justus Liebig University Giessen, Heinrich-Buff-Ring 17, 35392 Giessen, Germany. E-mail: Marcus.Rohnke@phys.chemie.uni-giessen.de; Fax: +49 641 99 34509; Tel: +49 641 99 34502*

[b]*Experimental Trauma Surgery, Faculty of Medicine, Justus Liebig University Giessen, Aulweg 128, 35392 Giessen, Germany*

† Electronic supplementary information (ESI) available. See DOI: https://doi.org/10.1039/d2an00913g

tion of up to 50 nm,[22] this method has successfully been used in numerous studies regarding biomaterials in context of osteoporosis. For example, ToF-SIMS enabled monitoring the release and incorporation of active substances into bone,[4,8,21,23,24] or chemical characterisation of biomaterial/bone interfaces,[25–28] bone cells[29] as well as bone mineral status.[30–32]

In addition to strontium mobility in the mineralised parts of bone, knowledge of strontium mobility in bone marrow is essential. However, the study of strontium diffusion in bone marrow is non-trivial due to its complex composition.[33–37] Bone marrow is a highly viscous, lipid-rich, and water-containing tissue,[36,38–40] which makes the experimental determination of the diffusion of Sr^{2+} challenging. Therefore, in a previous study, we first developed and evaluated a suitable ToF-SIMS measurement protocol for the determination of the diffusion coefficient of Sr^{2+} in bovine bone marrow in a passive transport model.[41] For this initial approach, we chose easily and inexpensively accessible bovine bone marrow and developed a special experimental protocol in which ToF-SIMS depth profile analyses of Sr^{2+} diffusion were performed under cryogenic conditions.[41] In a time-dependent experimental series, we determined the diffusion coefficients for Sr^{2+} in bovine bone marrow and thus, demonstrated the validity of our experimental approach. Furthermore, 2D and 3D ToF-SIMS imaging analyses of Sr^{2+} diffusion in bovine bone marrow showed that it does not occur homogeneously. We observed faster Sr^{2+} diffusion in bone marrow areas correlated with lower intensity of lipid and fatty acid signals. In the present proof-of-concept study, we focus on the determination of Sr^{2+} diffusion in the bone marrow of osteoporotic rats, based on the previously developed protocol for a passive transport model in bovine bone marrow.[41] Bone marrow is primarily composed of lipids, with the lipid as well as the fatty acid composition of the total bone marrow lipid content varying depending on animal species, age, diet, and tissue location.[36,42–48] Nevertheless, palmitic acid, stearic acid, and oleic acid are predominate in both rat and bovine bone marrow.[44,46,48–50] Furthermore, bone marrow fat consists mainly of triacylglycerides, and phosphatidylcholine is the major phospholipid of rat and bovine bone marrow.[42,44,48,50–52] Due to these similarities in bone marrow composition, we state that the experimental approach for determining strontium diffusion in bovine bone marrow should also be suitable for determining strontium diffusion in rat bone marrow.

High-resolution 2D imaging analysis using cryo-ToF-SIMS is applied to study Sr^{2+} distribution on rat bone marrow surface. ToF-SIMS imaging results are compared to histological staining of bone sections with Sudan Black B. 3D imaging analysis as well as depth profiling using cryo-ToF-SIMS are applied to study Sr^{2+} diffusion within the bone marrow bulk of bone sections. Thus, we determine Sr^{2+} transport properties for the first time in bone sections in a biologically passive but spatially intact environment. Furthermore, we perform cryo-OrbiSIMS analyses of Sr^{2+} diffusion into rat bone marrow and pure rat fat sections with the recently developed M6 Hybrid SIMS (IONTOF GmbH). Here, OrbiSIMS combines high mass resolving power (<240 000 at m/z 200) with high mass accuracy and thus allows unambiguous peak identification and distinction of different ion species in highly complex organic samples.[53]

2. Experimental

2.1 Preparation of cryo-sectioned rat bone and rat fat samples

Animal experiments were approved by and performed in full compliance with the institutional and German protection laws and the local animal welfare committee (Reference number: V 54–19 c 20-15 (1) GI 20/28 No. 108/2011). 10 weeks old healthy female Sprague-Dawley rats with an initial weight of 250–290 gram were purchased from Charles River (Sulzfeld, Germany). Animals underwent an acclimatisation period of four weeks in filter-topped plastic cages (2–4 rats per cage) with free access to water and food. After four weeks, an osteoporotic bone status (OVX) was induced by bilateral ovariectomy combined with a multi-deficient diet free of calcium, phosphorus, vitamin D3, soy, and phytoestrogen (Altromin-C1034, Altromin Spezialfutter GmbH, Lage, Germany) (Table S1†) as previously described.[4] Animals were euthanised 18 weeks post-ovariectomy under inhalation of CO_2 after general anesthesia. Osteoporotic status was shown by μ-CT measurements.[8] Right femura of OVX rats were harvested for cryo-sectioning by removing of all surrounding soft tissue. Afterwards, bones were frozen at −80 °C until they were embedded.

Fat of rats were harvested for cryo-sectioning. Approximately 24 hours prior the embedding procedure, rat femur and fat samples were thawed and prefixed with 4% paraformaldehyde (Carl Roth, Karlsruhe, Germany). For embedding procedure, acetone was added to dry ice in a cold tolerant liquid nitrogen container. Hexane was poured into a cold tolerant beaker, which was then placed in the dry ice-acetone container in a way that hexane in the inside and acetone in the outside of the beaker had the same height. Prefixed bone and fat samples were placed in a stainless-steel mold and SCEM-L1 embedding medium (SECTION-LAB Co., Hiroshima, Japan) was added to the samples. The filled mold was placed into the hexane containing beaker until the embedding medium was completely solidified. Embedded bone and fat sample blocks were carefully removed from the stainless-steel mold, wrapped in aluminium foil, and stored at −80 °C until sectioning.

Cryo-sectioning of embedded rat bone and fat was performed according to Schaepe *et al.*,[54] with a cryostat CM 3050 S (Leica, Nussloch, Germany). Specimen temperature was −30 °C and cryo-chamber temperature was −20 °C. Blade holder, SL-30 tungsten carbide blades, and cryo-film tapes of type 2C(9) were purchased from SECTION-LAB Co. (Hiroshima, Japan). After cutting of at least 15 μm thick sections, bone sections as well as fat sections were mounted on aluminium slides and stored at −80 °C until analysis.

2.2 Diffusion experiments

Diffusion experimental protocol was adapted from Kern *et al.*[41] Bone sections and rat fat sections were slowly thawed

in air to room temperature prior to diffusion experiments. Samples were then adapted to a heating/cooling sample holder from IONTOF GmbH (Muenster, Germany) to enable continuous sample cooling during measurement. To ensure good cold transfer, the aluminium sample carrier was attached to the sample holder *via* adhesive copper tape. Aqueous $SrCl_2$ solution (c = 1 mol l^{-1}) was dropped onto rat bone and rat fat sections (Fig. 1A). Residence times of $SrCl_2$ solution on samples was 10 s to 25 s at room temperature. Afterwards, $SrCl_2$ was removed from the sample surface and samples were immediately introduced into the load lock of the TOF.SIMS 5 instrument (IONTOF GmbH) where the diffusion process was stopped by cooling samples down with liquid nitrogen. For determination of Sr^{2+} diffusion, the diffusion time t in eqn (3) was chosen as the addition of the residence time of $SrCl_2$ solution on bone marrow and the time point until the sample reached a temperature below 10 °C in the prechamber as previously described.[41] Further details are explained in the ESI.† Evacuation to vacuum was started after reaching 0 °C in the load lock and samples were then transferred to the main chamber of the TOF.SIMS 5 instrument. There, samples were further cooled with liquid nitrogen to prevent Sr^{2+} diffusion and temperature was kept below −120 °C during the entire analyses.

2.3 Depth profiling with ToF.SIMS 5 (IONTOF GmbH, Muenster, Germany)

Depth profiling analyses were performed with a ToF.SIMS 5 instrument (IONTOF GmbH, Muenster, Germany). The measurements were carried out in the positive ion mode and charge compensation was done with a low energy electron flood gun. Depth profiling of rat bone marrow was performed in the non-interlaced mode (Fig. 1B). The primary ion gun was operated in the spectrometry (high-current bunched) mode. As analysis species, 25 keV Bi_3^+ ion clusters were used, with primary ion currents between 0.2–0.4 pA. Scanning was performed in sawtooth mode with 100 µs cycle time, 128 × 128 pixels, 1 shot/frame/pixel and 1 frames/patch. The obtained mass resolution $m/\Delta m$ (FWHM) was for all measurements above 3000 at peak m/z $C_5H_9^+$. After each analysis scan, sample surface was sputtered for 10 s with 10 keV Ar_{1500}^+ ions with sputter currents between 8 and 13 nA. Sputter pause was 5 s. Sputter beam area was 350 × 350 µm^2. The subsequent analysis area (100 × 100 µm^2) was centred in the sputter area in order to avoid crater-wall-effects. Internal mass calibration was performed using H^+, H_2^+, CH_3^+, CH_4N^+, $C_2H_5^+$, $C_3H_7^+$, and $C_4H_8N^+$ mass signals in positive ion mode.

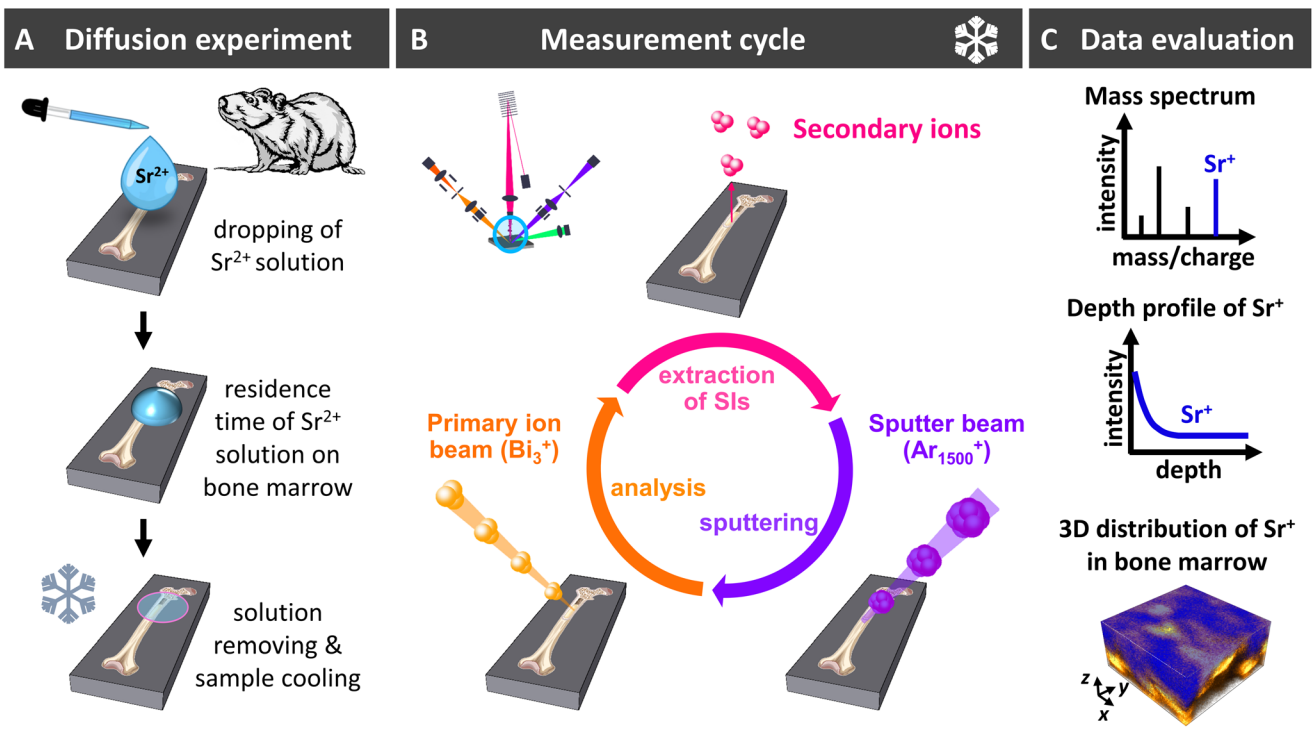

Fig. 1 Schematic representation of Sr^{2+} diffusion experiments with cryo-ToF-SIMS. (A) Aqueous $SrCl_2$ solution is dropped onto the surface of cryo-bone sections from osteoporotic rats. After 10 s to 25 s of residence time on the sample surface, strontium solution is removed. Bone sections are immediately cooled down using liquid nitrogen to prevent further Sr^{2+} diffusion into the bone marrow. (B) Principle of depth profiling in dual-beam ToF-SIMS mode. Measurement cycle starts with analysis of the bone section surface by an primary ion beam, generating secondary ions (SIs). SIs are extracted into the analyser, leading to locally-resolved mass spectra. A sputter beam is applied in the third step to remove the sample surface layer, thus creating a crater which is typically 2–3 times larger than the analysis area. The measurement cycle is repeated until the desired depth of the sample is reached. (C) By selecting a signal of interest (*e.g.*, Sr^+) in the mass spectrum, the depth profile of the selected signal and its 3D distribution in the analysis volume are obtained. Experimental protocol is adapted from Kern *et al.*[41]

After depth profiling, each sputter crater depth was determined with a confocal microscope PLu neox 3D (Sensofar, Terrassa, Spain). The obtained depth was used to calibrate the sputter time axis and to determine the erosion rate. We assumed a constant erosion rate for all measurements of rat bone marrow for the calibration of the depth profiles. Data analysis of the ToF-SIMS measurements was done with Surface Lab Software version 7.2 (IONTOF GmbH, Muenster, Germany) (Fig. 1C). For determination of Sr^{2+} diffusion in rat bone marrow, diffusion experiments were performed on two rat bone sections each from two different rats (on each section, two depth profiles were measured; total number of diffusion experiments was $n = 8$).

2.4 Imaging analysis with M6 hybrid SIMS (IONTOF GmbH, Muenster, Germany)

High-resolution mass spectrometric imaging analyses of Sr^{2+} diffusion into cryo bone sections of osteoporotic rat (Fig. 4C, 5 and Fig. S2†) and rat fat sections (Fig. 8 and Fig. S3†) as well as overview 2D image of whole rat bone section (Fig. 4B) were performed with a M6 Hybrid SIMS instrument (IONTOF GmbH, Muenster, Germany). The M6 Hybrid SIMS is equipped with both a ToF analyser and an OrbiTrap™ analyser. For high lateral resolution imaging analysis of bone sections, the ToF analyser was used. All measurements were carried out in the positive ion mode and as analysis species, 30 keV Bi_3^+ ion clusters were used as primary ion species. During the entire measurements, argon gas flooding and low energy electron flood gun were applied for charge compensation. For all measurements, the IONTOF heating/cooling sample holder was used and the sample temperature was kept below −120 °C during measurements.

Overview 2D image of a whole rat bone section (Fig. 4B) was obtained by large area scan (6.5 × 12.5 mm^2) in the spectrometry mode (high-current, bunched mode). Scanning was performed in sawtooth mode with following parameters: 3 shots per pixel, 3 frames per patch of 400 × 400 μm^2 and 350 pixels per mm pixel density, cycle time 100 µs, 3 scans, primary ion current of 0.8 pA. Following signals were used for internal mass calibration: $C_2H_5^+$, $C_3H_5^+$, $C_3H_7^+$, $C_5H_9^+$, $C_5H_{12}N^+$, and $C_{16}H_{31}O^+$. Obtained mass resolution $m/\Delta m$ (FWHM) was for all measurements better than 5000 for the $C_7H_{13}^+$ mass signal.

High-lateral resolution 2D images were obtained in the delayed extraction mode (delay times 150 ns, respectively). Measurements were performed in the sawtooth mode with parameters for rat bone sections listed in Table 1 (Fig. 4C, 5 and Fig. S2†) and rat fat sections listed in Table S2† (Fig. 8 and Fig. S3†). Following signals were used for internal mass calibration: $C_2H_5^+$, $C_3H_5^+$, $C_3H_7^+$, $C_5H_9^+$, $C_5H_{12}N^+$, and $C_{16}H_{31}O^+$. Obtained mass resolution $m/\Delta m$ (FWHM) was for all measurements better than 5000 for the $C_7H_{13}^+$ mass signal.

For Orbitrap imaging and spectral analysis (Fig. 6, 7 and 9), the OrbiTrap™ analyser was used. Orbitrap mass calibration was performed once a day at the beginning of a measurement session on a silver plate, following the calibration protocol described by Passarelli *et al.*[53] For calibration, the LMIG (30 keV Bi_3^+) was used with the 400 µm aperture and 20% long pulses together with the ThermoFisher Tune software. As the mass calibration remains stable for >25 h, no recalibration for data analysis afterwards was necessary. For Orbitrap imaging and spectral analyses, Ar_{3000}^+ cluster ions with 20 keV were used as primary ions. Measurement parameters are listed in Table 2.

Data analysis of M6 Hybrid SIMS measurements was done with Surface Lab Software version 7.2 (IONTOF GmbH, Muenster, Germany).

2.5 Histological staining of bone sections

Sudan Black B staining system (Sigma-Aldrich, St. Louis, MO) was performed on frozen bone sections to identify various lipids and fat droplets (Fig. 7), according to Davey *et al.*[55] Rat adipose tissue was used as positive control. Sections were first immersion fixed with glutaraldeyde fixative solution for 1 min at 2–8 °C with gentle agitation followed by staining in Sudan Black B staining reagent for histology. Images were taken using a Leica microscopy system (Leica DM5500 photomicroscope equipped with a DFC7000 camera and operated by LASX software version 3.0, Leica Microsystem Ltd, Wetzlar, Germany). Fiji ImageJ (version 1.51r; NIH,) was used for histomorphometry measurements of Sudan Black B sections as previously described.[56]

2.6 Statistical analysis

Mean of diffusion coefficient values from repeated tests were analysed using Mann–Whitney U-test after ascertaining a non-

Table 1 Parameters for ToF-SIMS delayed extraction imaging of Sr^{2+} diffusion into bone marrow of osteoporotic rat bone (Fig. 4, 5 and Fig. S2†) obtained in positive ion mode with M6 Hybrid SIMS (IONTOF GmbH, Muenster, Germany)

Fig. Analysis options	4C	S2(A–D†)	S2(E–H†)	S2(I and J†), 5
Cycle time	120 µs	120 µs	120 µs	120 µs
Field of view	150 × 150 μm^2	300 × 300 μm^2	150 × 150 μm^2	50 × 50 μm^2
Primary ion current	0.08 pA	0.06 pA	0.06 pA	0.06 pA
Pixels	1024 × 1024	2048 × 2048	1024 × 1024	512 × 512
Frame per patch	1	1	1	1
Primary ion shots/frame/pixel	2	1	1	1
Number of scans	100	8	51	180

Table 2 Parameters for Orbitrap imaging of Sr^{2+} diffusion into rat bone sections (Fig. 6 and 7) and rat fat sections (Fig. 9) obtained in positive ion mode with M6 Hybrid SIMS (IONTOF GmbH, Muenster, Germany)

Fig. Analysis options	6	7D	7E	9
Cycle time	160 μs	160 μs	160 μs	130 μs
Raster mode	Random	Random	Random	Random
Field of view	400 × 400 μm^2	400 × 400 μm^2	50 × 50 μm^2	400 × 400 μm^2
Primary ion current	60 pA	58 pA	58 pA	61 pA
Pixel size	8 μm	8 μm	2 μm	5 μm
Spot size	5 μm	5 μm	2 μm	5 μm
Border size	2 μm	2 μm	2 μm	2 μm
Mass resolution	240 000	240 000	240 000	60 000
Mass range	*m*/*z* 80-1,200	*m*/*z* 80-1,200	*m*/*z* 80-1,200	*m*/*z* 80-1,200
Injection time	500 ms	500 ms	500 ms	100 ms
Number of scans	2	2	2	2

normal distribution with a Shapiro–Wilk test or one-way ANOVA after ascertaining a normal distribution. Diffusion coefficients are reported as means ± standard deviation STD. Statistical analyses were performed using Origin v9.3 (OriginLab Corporation, Northampton, MA, USA). Multivariate Statistical Analysis (MVSA) in form of Principal Component Analysis (PCA) was performed using Surface Lab Software version 7.2 (IONTOF GmbH, Muenster, Germany). For the MVSA calculation, 2D-images were used as data type and PCA as MVSA method. As source data options, corrected data and lateral shift correction were chosen, without XY or Z pixel binning. After mass calibration of the mass spectra, FA, lipid as well as strontium fragment ion peaks were selected as source intervals for PCA. Following calculation options for PCA, recommended by the software as default, were applied: none spatial scaling, empirical spectral scaling, and none centering.

3. Results

3.1 Determination of Sr^{2+} diffusion coefficients in rat bone marrow

Since determination of Sr^{2+} diffusion in bovine bone marrow was successful in our previous study,[41] we adapted the developed experimental protocol for the determination of Sr^{2+} diffusion in rat bone marrow of osteoporotic rats (Fig. 1). Rat bone sections were prepared *via* cryo-sectioning of cryo-embedded bone samples to preserve the lipid content of the bone marrow. As rat bone sections were only 15–40 μm thick, the experimental procedure was slightly modified by reducing the residence time of the aqueous $SrCl_2$ solution on bone sections to 10–25 s (Fig. 1A).[41] After this short deposition time, strontium solution was removed and further diffusion was stopped by freezing of the tissue. ToF-SIMS depth profiling under cryogenic conditions (Fig. 1B) was then applied for characterisation of Sr^{2+} distribution. Here, in the first step of a repeating measurement cycle, secondary ions (SIs) are produced by a pulsed primary ion beam. The SIs are then extracted and analysed in a time-of-flight mass analyser in the second step. During the third step the sample surface layer is removed by applying a sputter ion beam. The measurement cycle with alternating analysing and sputtering steps finally results in mass spectra, diffusion profiles, and 3D mass image maps (Fig. 1C). Depth profiling was conducted in positive ion mode since strontium forms predominately positive secondary ions in SIMS analyses.[57] It also has to be noted that the obtained secondary ions are primarily single charged, despite of their +II oxidation state within the sample. Hence, diffusion profiles of the Sr^+ signal were used for evaluation of Sr^{2+}diffusion coefficients in rat bone marrow.

In order to determine diffusion coefficients of Sr^{2+} diffusion in bone marrow of osteoporotic rats, a mathematical solution of Fick's second diffusion law (eqn (1)) has to be fitted to the obtained Sr^+ depth profiles (Fig. 2).

$$\frac{\delta c}{\delta t} = \frac{\delta}{\delta x}\left[D\frac{\delta c}{\delta x}\right] \quad (1)$$

In our previous study, for Sr^{2+} transport in bovine bone marrow, we assumed diffusion from an exhaustless source into semi-infinite space as boundary conditions for solving Fick's second law of diffusion (eqn (2), fit model 1).[41]

$$I(x) = I_{bg} + I_0 \cdot \left(1 - \mathrm{erf}\frac{x - x_0}{2\sqrt{Dt}}\right) \quad (2)$$

I_{bg} = background intensity of Sr^+ in bone marrow; I_0 = initial intensity of the infinite source; x = position/depth; x_0 = starting point of the diffusion profile (bone marrow surface); D = diffusion coefficient; t = diffusion time

However, in the present study, due to the shorter residence time of $SrCl_2$ on rat bone marrow, diffusion from an exhaustless source cannot longer be assumed but rather the diffusion of a given amount of Sr^{2+} (I_0) deposited on a certain area A of bone marrow.[58,59] For solving Fick's second law of diffusion (eqn (1)) for Sr^{2+} diffusion in rat bone marrow, different boundary conditions for the spatial variables and an initial condition for the time and therefore, a different diffusion model had to be defined for this case of instantaneous plane source diffusion.[58,60]

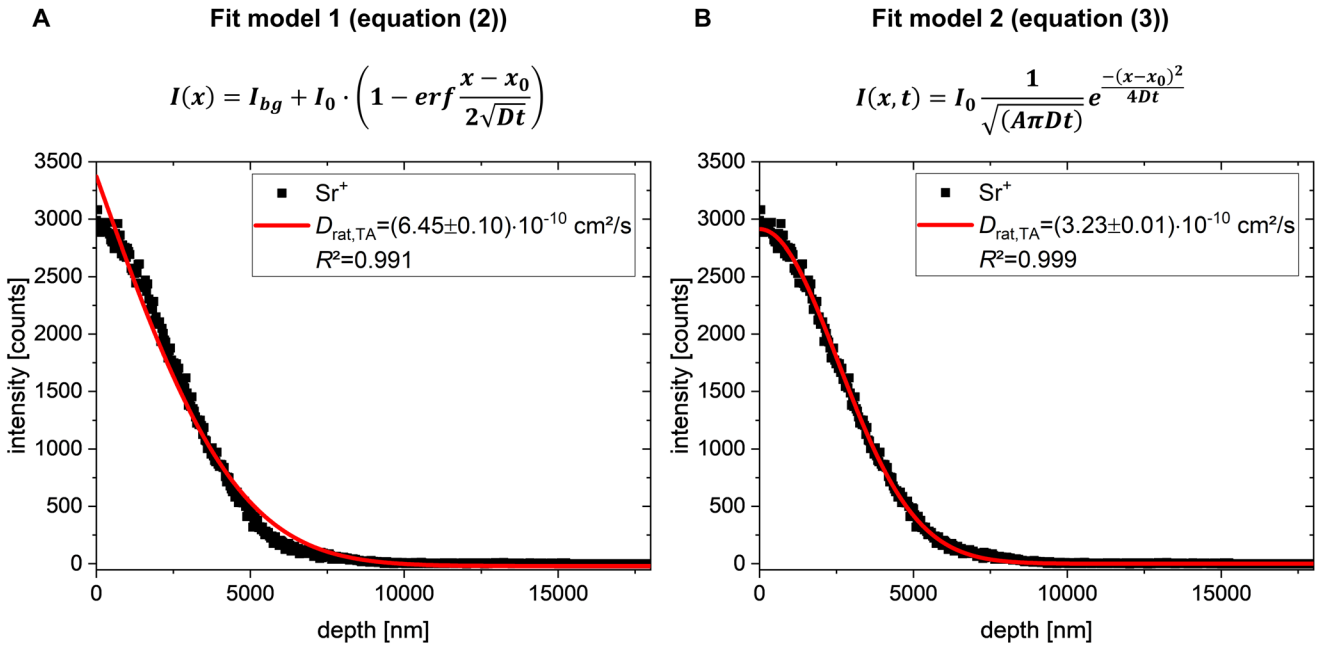

Fig. 2 Comparison of (A) diffusion fit model 1 (eqn (2)) and (B) diffusion fit model 2 (eqn (3)) for Sr^{2+} diffusion into rat bone marrow. Solid red lines in (A) and (B) represent the results of the mathematical fitting performed according to (A) eqn (2) and (B) eqn (3), respectively. For all depth profiles, Bi_3^+ primary ions (25 keV) were used for analysis with the TOF.SIMS 5. Sputtering was done with a 10 keV Ar_{1500}^+ cluster beam.

(a) At $t = 0$ and $x_0 = 0$, the total amount of diffusive species (Sr^{2+} ions, I_0) is deposited within an area A in the yz-plane of the semi-infinite bone marrow.

(b) Concentration of the Sr^{2+} ions is the same over the entire area A.

(c) Total amount of the diffusive species is always I_0 and therefore equal to the amount of originally deposited Sr^{2+} ions in the yz-plane.

Solving eqn (1) with the defined boundary and initial conditions, following expression (eqn (3), fit model 2) has been yielded as a function of time t and position x:

$$I(x,t) = I_0 \frac{1}{\sqrt{(A\pi Dt)}} e^{\frac{-(x-x_0)^2}{4Dt}} \quad (3)$$

I_0 = initial intensity of the deposited amount of Sr^{2+} ions at t = 0 and x_0 = 0; A = area of deposited amount of Sr^{2+} ions; x = position/depth; x_0 = starting point of the diffusion profile; D = diffusion coefficient; t = diffusion time

Furthermore, following assumptions were made:

(a) Diffusion coefficient of Sr^{2+} is constant (evaluated by the time-dependent experimental series of strontium diffusion in bovine bone marrow[41]).

(b) Mathematical fits can be carried out with the obtained Sr^+ ion signal intensities since concentration c is proportional to secondary ion intensity I.

(c) There are no reactions of Sr^{2+} (diffusing species) with the rat bone marrow matrix and thus no sinks. No other sources of diffusing species are present throughout the observed diffusion process.

For determination of Sr^{2+} diffusion coefficients, mass spectrometric information of each analysis layer of cryo-ToF-SIMS depth profiles was summed up as intensity *versus* depth diffusion profiles (Fig. 2). Afterwards, the mathematical fit model 2 (eqn (3), Fig. 2B) was fitted to the measured ToF-SIMS diffusion profiles. The first data points were not considered for fitting the chosen solution of Fick's second law of diffusion to the experimental data since they may be influenced by sputter ion species as well as variable dopant concentrations of primary ions. To compare the two diffusion models, we also applied the diffusion fit model 1 (eqn (2), Fig. 2A), which was used for determination of the Sr^{2+} diffusion coefficient in bovine bone marrow,[41] to Sr^{2+} diffusion in rat bone marrow.

Both diffusion models provide diffusion coefficients within the same order of magnitude. Nevertheless, the experimentally obtained diffusion profile of strontium in rat bone marrow can be better described by the second fit model and the corresponding eqn (3) (Fig. 2B). For this reason, the diffusion profiles of Sr^{2+} in rat bone marrow were evaluated using the second fit model. An average diffusion coefficient of $D_{rat,TA}$= $(8.89 \pm 5.37) \times 10^{-10}$ cm^2 s^{-1} was obtained for Sr^{2+} diffusion in total measurement areas of rat bone marrow (n = 8, Fig. 3B).

Similar to the diffusion of Sr^{2+} in bovine bone marrow,[41] different diffusion areas in rat bone marrow could be determined by applying lateral Regions of Interest (ROIs) to 3D ToF-SIMS imaging data. Evaluation of the diffusion profiles from different regions of rat bone marrow revealed that the diffusion behaviour of Sr^{2+} in fast and slow regions differed only slightly (Fig. 3A). For fast diffusion (FD) areas, an average diffusion coefficient of $D_{rat,FD}$=$(9.05 \pm 5.64) \times 10^{-10}$ cm^2 s^{-1}

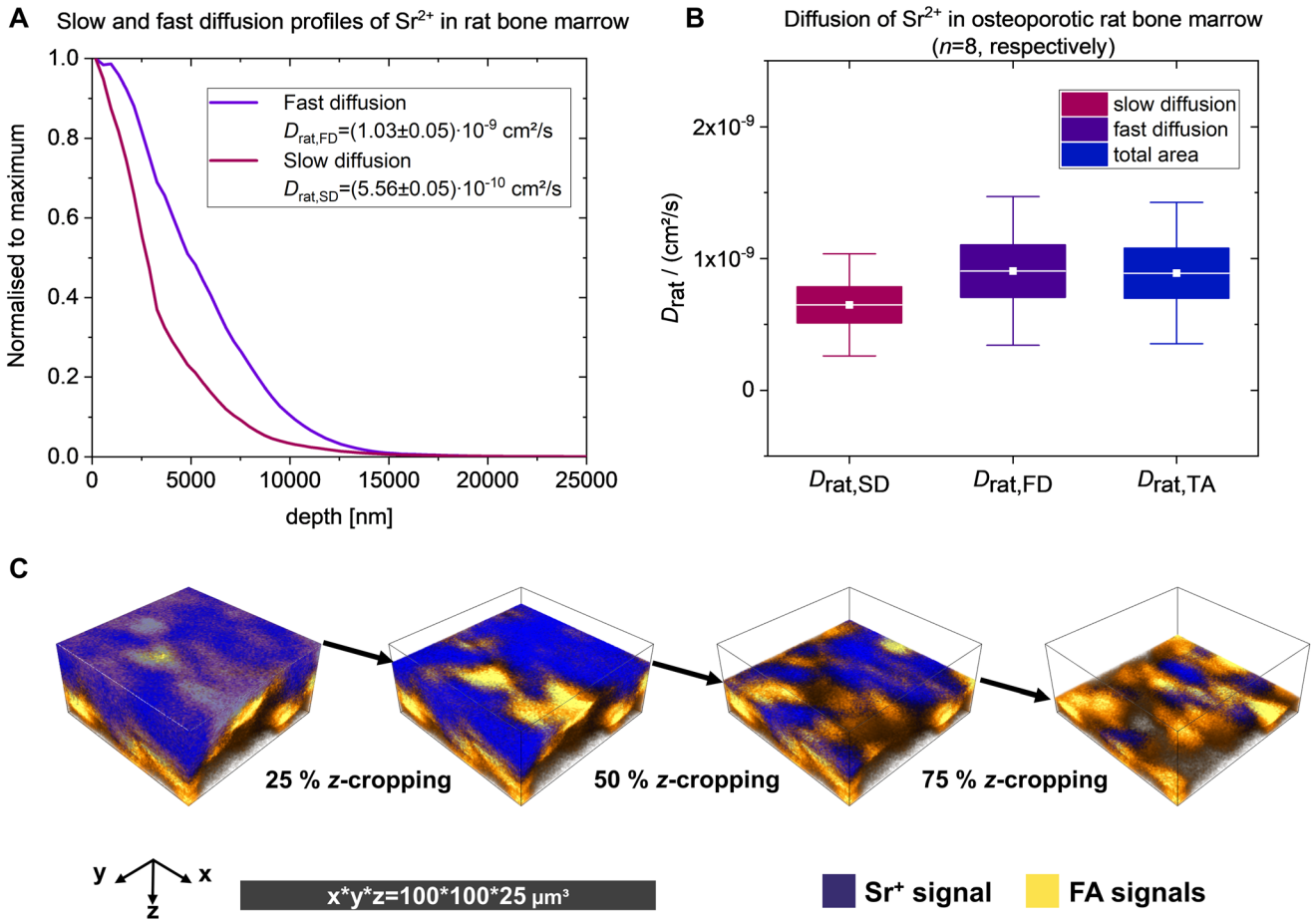

Fig. 3 (A) Diffusion profiles from areas of slow and fast diffusion show the in-depth distribution of Sr^{2+} in rat bone marrow (exemplarily presented by one measurement) in slow and fast diffusion areas. For comparison, strontium ion intensity was normalised to the maximum of each diffusion profile. (B) Experimentally obtained average diffusion coefficients of Sr^{2+} diffusion in rat bone marrow in slow diffusion areas ($D_{rat,SD}$), fast diffusion areas ($D_{rat,FD}$), and total diffusion areas ($D_{rat,TA}$) (n = 8, respectively; detailed values are listed in Table S4†). The mean diffusion coefficient of fast Sr^{2+} diffusion areas is non-significantly higher than the mean diffusion coefficient for areas of slow Sr^{2+} diffusion (one-way ANOVA test). Sr^{2+} diffusion in total measurement areas is mainly influenced by the fast diffusion and thus, also non-significantly faster than Sr^{2+} diffusion in slow diffusion areas (one-way ANOVA test). Values are presented as boxplots with mean value and interquartile range (25^{th} to 75^{th} percentile). Whiskers indicate maximum and minimum diffusion coefficient values. (C) Reconstructed 3D mass images of the corresponding diffusion profiles in (A) show strontium (blue) diffusion into rat bone marrow (yellow) at the surface, in the bulk at 25% z-cropping, at 50% z-cropping, and at 75% z-cropping. For 3D imaging analysis and diffusion profiles, 25 keV Bi_3^+ cluster primary ions were applied in spectrometry mode (positive ion mode, obtained with TOF.SIMS 5).

was obtained (n = 8, Fig. 3B). For slow diffusion (SD) areas, an average diffusion coefficient of $D_{rat,SD}=(6.48 \pm 3.88) \times 10^{-10}$ cm^2 s^{-1} was obtained (n = 8, Fig. 3B). Statistical evaluation (one-way ANOVA test, $*p < 0.05$) revealed a non-significant difference within the same order of magnitude between areas of fast and slow diffusion of Sr^{2+} into osteoporotic rat bone marrow (Fig. 3B). All diffusion coefficients for Sr^{2+} diffusion into rat bone marrow are listed in Table S4.†

The reconstructed 3D tomography (Fig. 3C) of the diffusion profile in Fig. 3A shows Sr^{2+} diffusion (blue) in rat bone marrow (displayed as fatty acid signals in yellow) at the surface as well as in depth at 25% z-cropping, at 50% z-cropping, and at 75% z-cropping (also shown in more detail in Fig. S2†). Strontium signals are mainly detected in areas of low fatty acid signal intensities, implicating slower Sr^{2+} diffusion in fatty acid and lipid rich areas. Fatty acid and lipid peaks are listed in Table S3.†

3.2 ToF-SIMS imaging of Sr^{2+} distribution in rat bone marrow

ToF-SIMS analyses showed Sr^{2+} diffusion mainly into areas of osteoporotic rat bone marrow with less intensity of secondary ions which derived from fatty acid and lipid species. High-resolution 2D image analysis on Sr^{2+} diffusion into rat bone sections using a Hybrid SIMS instrument allowed a detailed characterisation of the lateral Sr^{2+} distribution in rat bone marrow.

ToF-SIMS overview mass images of a femoral head (Fig. 4B) show mineralised bone in form of hydroxyapatite signals (HAP; mass signals used are listed in Table S5†). Bone marrow can be visualised with secondary ions derived from fatty acids (FA) and lipids (used mass signals are listed in Table S3†). Comparison of the mass images of HAP and

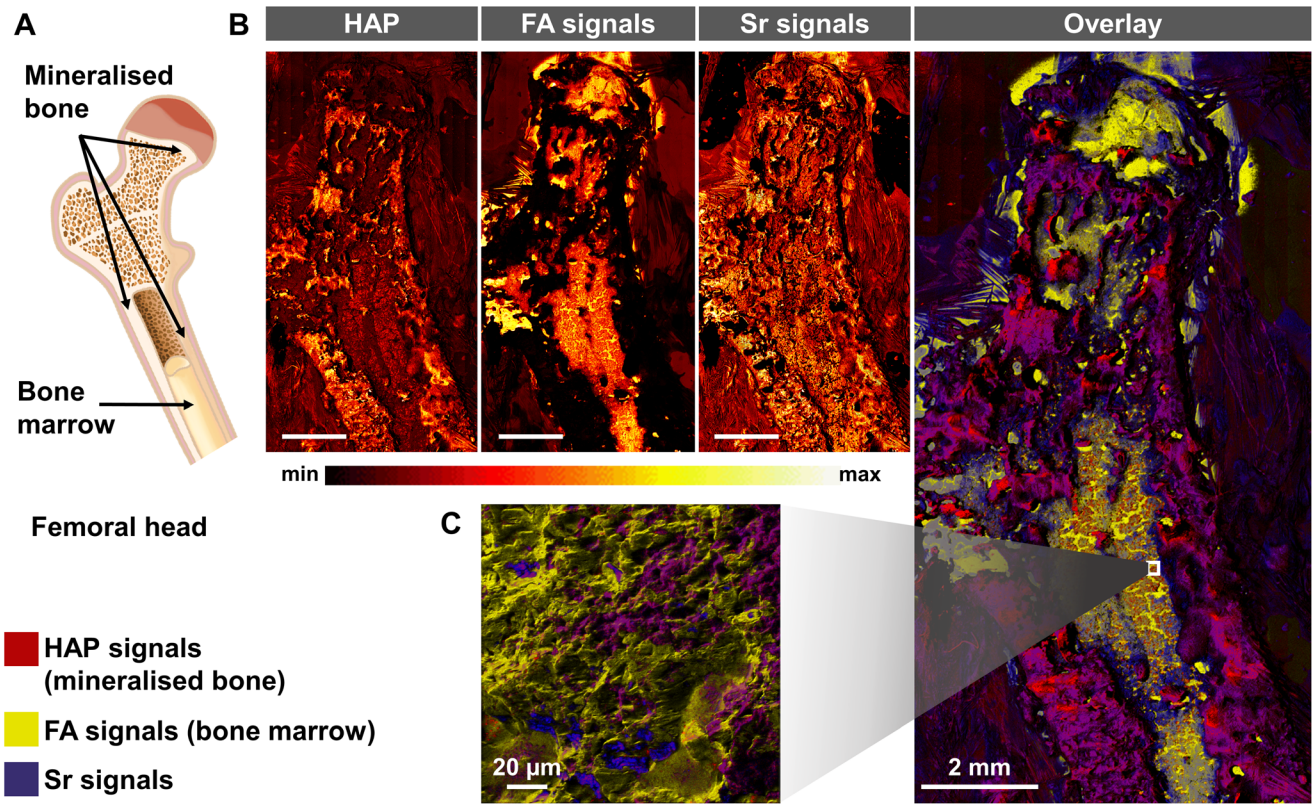

Fig. 4 2D ToF-SIMS image analysis of Sr^{2+} diffusion into a cryo-embedded rat bone section. (A) Schematic drawing of a femoral head showing mineralised bone as outer shell (cortical bone) and spongy, trabecular bone at the end of the femoral head. Bone marrow is located within the medullary cavity. (B) ToF-SIMS secondary ion images show mineralised bone in form of hydroxyapatite (HAP) signals, and bone marrow as secondary ions originating from fatty acid (FA) fragments. Comparison of the secondary ion images with the schematic of the femoral head from (A) indicates that HAP signals and FA signals are sufficient to represent mineralised bone and bone marrow, respectively. Lateral distribution of strontium signals shows that Sr^{2+} diffused into both mineralised bone region and bone marrow. Overlay image shows mineralised bone in red, bone marrow in yellow, and sum of strontium signals in blue. Areas with an overlap of strontium and HAP signals are shown in purple. (C) Detailed high-resolution image of an interface region of cortical bone and bone marrow shows strontium (blue) distribution mainly in areas of mineralised bone (red), and less in areas of high signal intensity of secondary ions which originated from FA fragments in bone marrow. High-resolution image was obtained with delayed extraction mode. 30 keV Bi_3^+ cluster primary ions were applied for (B) and (C) (positive ion mode, obtained with M6 Hybrid SIMS).

FA signals with a schematic drawing of a femoral head (Fig. 4A) show that HAP signals are sufficient for describing the mineralised bone and FA signals are sufficient for describing the bone marrow. Strontium signals (listed in Table S6†) are detectable both in the mineralised bone region as well as in the bone marrow. In the overlay image, purple areas indicate an overlap of strontium signals (blue) and mineralised bone (red). This can also be seen in the smaller and more detailed high-resolution image (Fig. 4C) of the interface of mineralised, cortical bone and bone marrow as well as high-resolution images of the bone marrow area (Fig. S3†). In areas of high signal intensity of fatty acid secondary ions (yellow), less intensity of strontium ion signals is detected.

For a statistical distinction of areas with high intensity of strontium signals and areas with high intensity of FA signals, a Principal Component Analysis (PCA) of the ion images of rat bone marrow from Fig. S3† was carried out. The results of the PCA analysis were compared to manually assigned areas for strontium and FA signals (Fig. 5). In PCA, each Principal Component (PC) describes a variance which is presented by loadings plot and image scores. Loadings illustrate which peaks contribute most to the variance described in each PC image. Positive loadings correspond to positive scoring pixels and negative loadings refer to mass fragments that are anti-correlated to the image score. The image scores in turn illustrate where the largest chemical variance was found, here by colouring positively scoring pixels in orange/red and negatively scoring pixels in blue. Therefore, loadings plots and image scores reveal peaks which are statistically responsible for the discrimination of different areas of the measured surface. PCA scores image of PC1 (Fig. 5D) shows positive loading fragments mainly found for fatty acid signals such as $C_2H_5^+$ (m/z 29.04), $C_3H_5^+$ (m/z 41.04), $C_3H_7^+$ (m/z 43.05), $C_4H_7^+$ (m/z 55.05), $C_4H_9^+$ (m/z 57.07), $C_5H_9^+$ (m/z 69.07), and $C_7H_{11}^+$ (m/z 95.09). Image scores for PC1 show the same pattern as the ion image of manually combined FA signals (Fig. 5A).

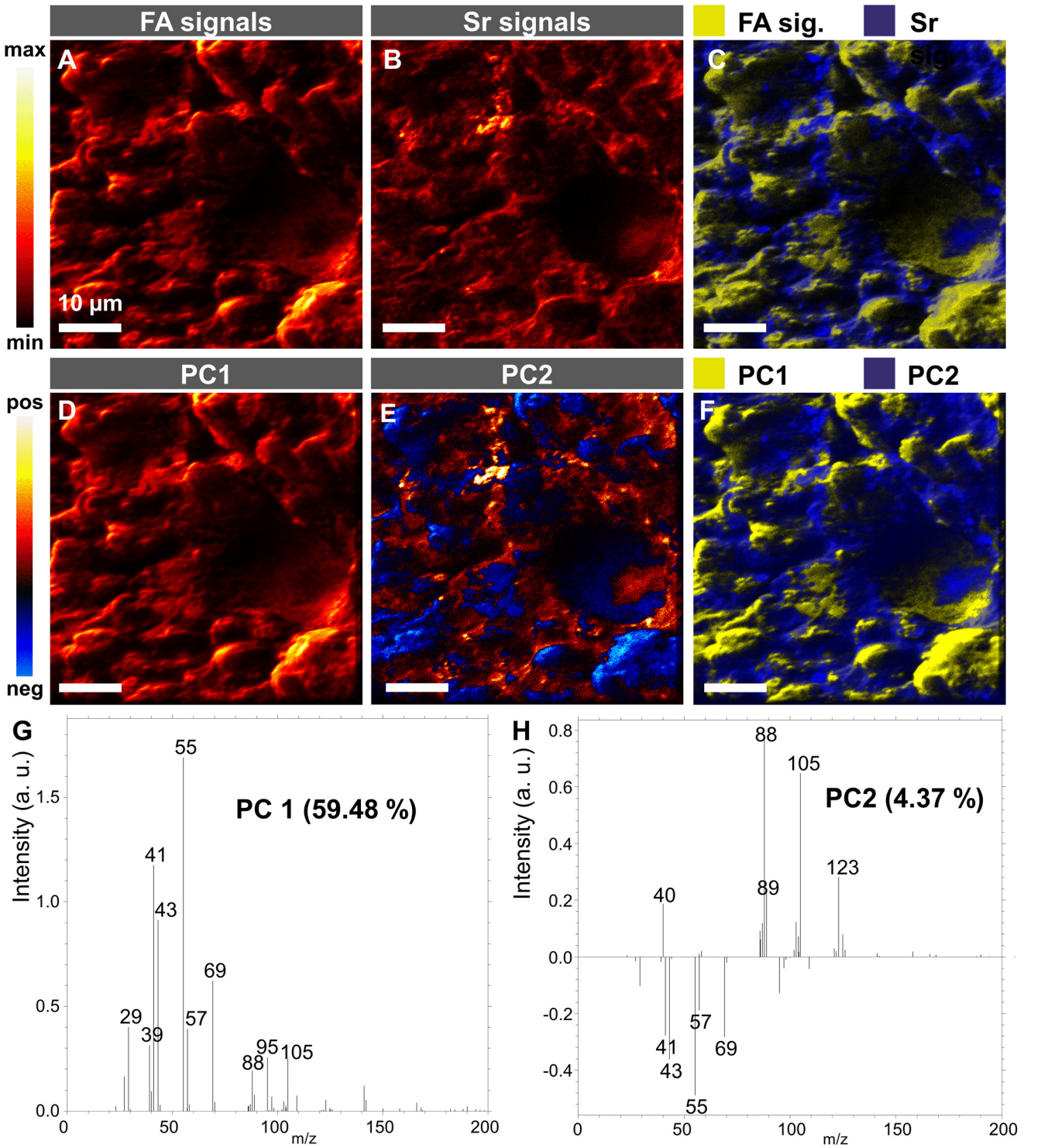

Fig. 5 PCA analysis of Sr^{2+} diffusion into rat bone marrow. Comparison of ToF-SIMS mass images of secondary ions originating from (A) fatty acid/lipid species, (B) strontium species, and (C) overlay of strontium signals (blue) and FA signals (yellow) with PCA scores images (D–F) and loadings plots (G and H). (D) PCA scores image of PC1 with (G) corresponding loadings plot. (E) PCA scores image of PC2 with (H) corresponding loadings plot. (F) Overlay image of PC1 (yellow) and positive loadings of PC2 in blue. 30 keV Bi_3^+ cluster primary ions were applied (positive ion mode, delayed extraction, obtained with M6 Hybrid SIMS).

In comparison, Fig. 5E shows the PCA scores image of PC2 with positive loading fragments (Fig. 5H) found for ion species such as Sr^+ (*m*/*z* 87.91), SrH^+ (*m*/*z* 88.91), $SrOH^+$ (*m*/*z* 104.91), and $SrCl^+$ (*m*/*z* 122.86). The pattern of positive loadings of PC2 (Fig. 5E, in orange/red) shows the same pattern as the ion image for manually combined strontium signals (Fig. 5B).

Negative loadings for PC2, shown in blue in the corresponding scores image (Fig. 5E), include mainly masses of fatty acid fragments. Therefore, FA mass fragments are anti-correlated to the PC2 scores image. Overlay of PC1 (yellow) and PC2 (blue) scores images (Fig. 5F) captures the variation between areas of fast strontium diffusion and high FA intensity and is comparable with the overlay of strontium (blue) and FA (yellow) signals (Fig. 5C).

In ToF-SIMS spectra, different ion flight times can occur due to topography effects, causing the ToF-SIMS peaks to broaden. Furthermore, deviations of the assigned mass from the theoretical mass of the fragments may occur due to the subsequent calibration of the mass spectra. Subsequent calibration is particularly challenging when one wishes to study both inorganic (strontium species in this case) and organic ion species. Thus, to obtain a mass spectrum with a higher mass resolution as well as better mass accuracy, the Hybrid SIMS instrument was operated with the OrbiTrap™ analyser. For analysis with the OrbiTrap™ analyser, GCIB was used (20 keV Ar_{3000}^+ clusters) as primary ion gun instead of LMIG.

First, an Orbitrap image was taken of a rat bone marrow area into which Sr^{2+} had diffused. After assigning strontium and FA/lipid signals, two different ROIs were selected. ROI 1 was in an area with high mass signal intensities of lipids and ROI 2 in an area with high intensities of strontium signals (Fig. 6A). The analysis of the obtained mass spectra showed a clear difference between ROI 1 and ROI 2 regarding the intensities of their mass signals (Fig. 6B). In ROI 1, mainly fragments of MAGs (*e.g.*, $C_{19}H_{35}O_3^+$ (*m*/*z* 311.2576), $C_{19}H_{37}O_3^+$ (*m*/*z* 313.2736), $C_{21}H_{39}O_3^+$ (*m*/*z* 339.2893), $C_{21}H_{41}O_3^+$ (*m*/*z* 341.3050); Fig. 6D) and DAGs (*e.g.*, $C_{33}H_{63}O_4^+$ (*m*/*z* 523.4718), $C_{35}H_{67}O_4^+$ (*m*/*z* 551.5032), $C_{37}H_{67}O_4^+$ (*m*/*z* 575.5033), $C_{37}H_{69}O_4^+$ (*m*/*z* 577.5188), $C_{37}H_{71}O_4^+$ (*m*/*z* 579.5344); Fig. 6E) were detectable with higher signal intensities than in the mass spectrum of ROI 2. In contrast, strontium signals show higher signal intensity in ROI 2 than in ROI 1 (Fig. 6C).

In order to verify our interpretation of the ToF- and OrbiSIMS analyses, the same rat bone sections were afterwards stained with Sudan Black B for a comparable histological analysis. Sudan Black B is a fat-soluble dye with a very high affinity

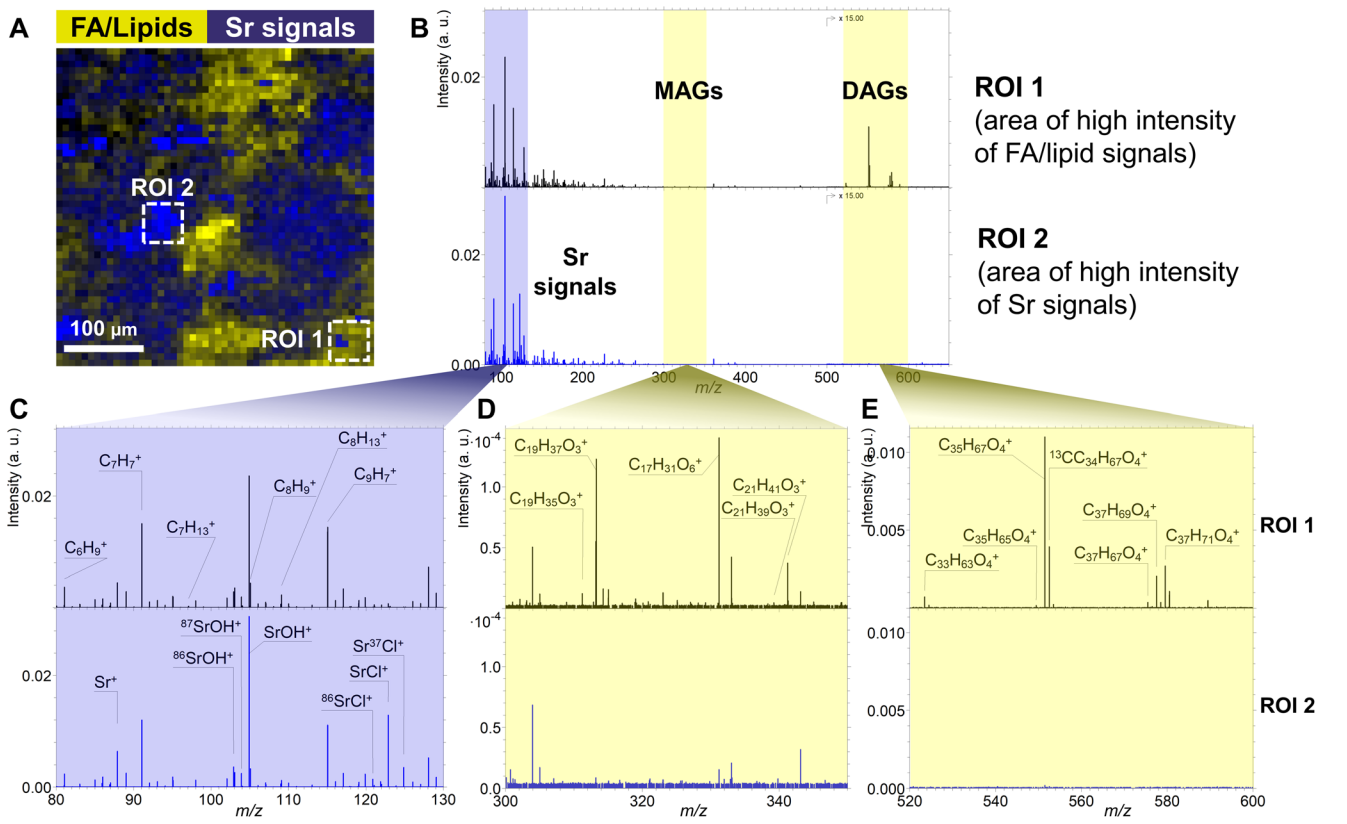

Fig. 6 Analysis of Sr^{2+} diffusion into rat bone marrow of osteoporotic rat using the OrbiTrap™ analyser. (A) Overlay of ion image of FA/lipid signals (yellow) and strontium signals (blue). Dotted boxes show the chosen areas of ROI 1 and ROI 2. ROI 1 is in an area with high intensity of fatty acid and lipid mass signals. ROI 2 is in an area with high intensity of strontium signals. (B) Positive mass spectra of ROI 1 and ROI 2 in a mass range of *m*/*z* 80–650. Mass ranges with signals from lipids (MAGs, DAGs) are marked in yellow. Mass range with strontium signals is marked in blue. (C) Detailed mass range of *m*/*z* 80–130 shows higher intensities of strontium signals in ROI 2 than in ROI 1. (D) Detailed mass range of *m*/*z* 300–350 shows higher intensities of mass fragments derived from MAGs in ROI 1 than in ROI 2. (E) Detailed mass range of *m*/*z* 520–600 shows higher intensities of mass fragments derived from DAGs in ROI 1 than in ROI 2. For comparison of the peak intensities, the spectra were normalised to the total counts (scale spectra by total counts). Identified peaks are listed in Table S3.† For Orbitrap imaging and spectral analysis, 20 keV Ar_{3000}^+ cluster primary ions were applied (positive ion mode, obtained with M6 Hybrid SIMS).

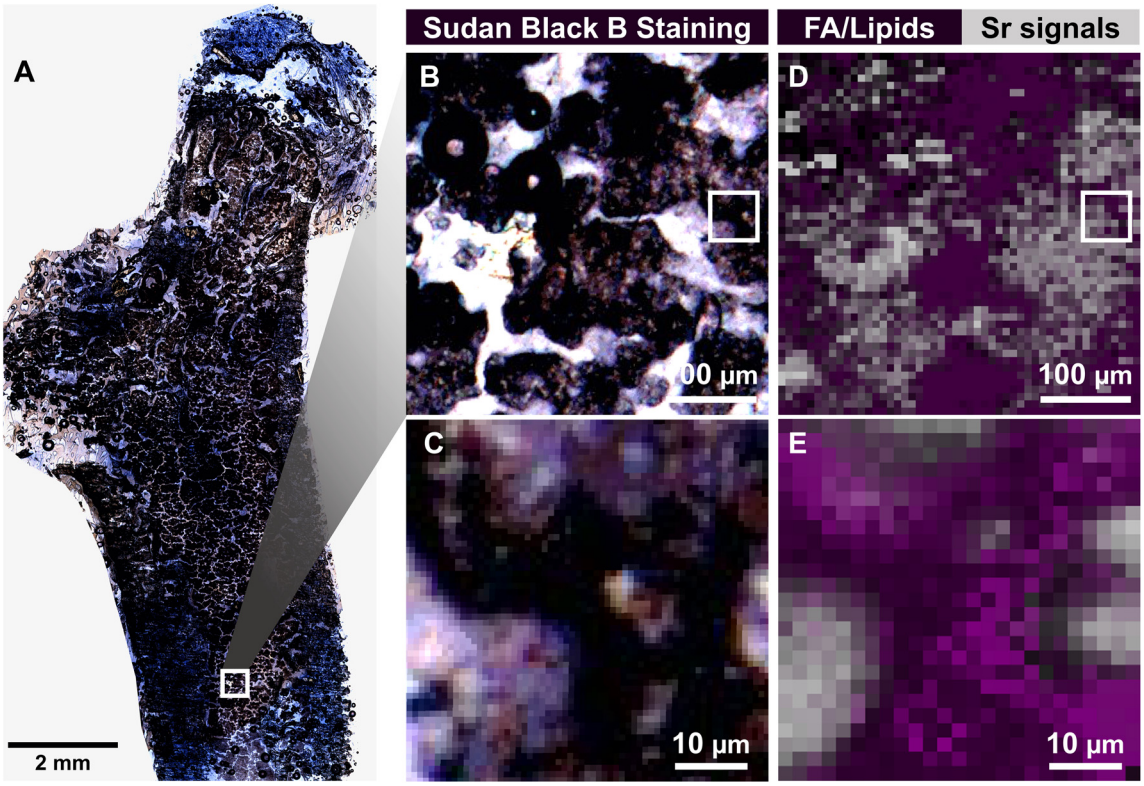

Fig. 7 Comparison of histological staining and OrbiSIMS imaging analysis of rat bone marrow. (A) Overview image of rat bone femur stained with Sudan Black B. (B) Higher magnification of Sudan Black B stain in the bone marrow, showing stain affinity to lipids and fat droplets (dark purple to black color). Empty areas (light purple to white color) indicate no binding of Sudan Black B. (C) A digital zoom shows that lipids at cell walls stained with higher affinity (black) than fat droplets (purple). (D and E) Overlay of corresponding ion mass images show FA/lipid signals in purple and strontium signals in grey. For Orbitrap imaging analysis, 20 keV Ar_{3000}^+ cluster primary ions were applied (positive ion mode, obtained with M6 Hybrid SIMS).

for neutral fats and lipids, thus staining unspecifically several lipids, phospholipids, neutral fats, and sterols intensely. Fats and lipids throughout the stained bone section are shown in a dark purplish-blue to black in areas of both bone marrow and mineralised bone (Fig. 7A). Sudan Black B binds with higher affinity to the phospholipids in cell membranes and to granules in monocytes. These lipids are exposed, which is why the staining takes on a black color after differentiation. Lipid droplets such as triglycerides respond differently to staining and are dark purple. Detailed analysis areas of bone marrow show good agreement between lipids stained with Sudan Black B in the histology image (Fig. 7B and D) and the results of OrbiSIMS imaging analysis (Fig. 7C and E). Here, ion fragments originating from lipids and FAs are shown in purple for better comparison with the histological staining. Spatial distribution of the lipid/FA signals in the OrbiSIMS mass image is comparable to their distribution shown in the histological staining. Strontium signals, on the other hand, are in areas that were not stained using Sudan Black B.

3.3 Sr^{2+} diffusion in rat fat sections

In both bovine bone marrow[41] and osteoporotic rat bone marrow, we observed that strontium ion species have lower signal intensities in areas with high signal intensities of fatty acids and lipids, and *vice versa*. For further investigation of Sr^{2+} diffusion into fat-rich areas, diffusion of Sr^{2+} into fat sections of rats was characterised. Since these fat sections are mainly composed of adipocytes, they are suitable for the investigation of Sr^{2+} diffusion into fat cells.

High-resolution mass images (Fig. 8) of areas of rat fat sections were obtained with the Hybrid SIMS using the delayed extraction ToF-SIMS mode. Secondary ions which derived from fatty acids (Fig. 8C and G; yellow in the overlay images Fig. 8A and E) as well as from MAGs/DAGs (Fig. 8D and H) show shapes of adipocytes and a complementary lateral distribution to strontium signals (Fig. 8B and F; blue in the overlay images Fig. 8A and E). Same as in bone marrow, strontium signals in rat fat sections are detectable with higher intensity in areas where the intensity of FA signals is low and *vice versa*. Used mass signals for FAs, MAGs, and DAGs are listed in Table S3,† strontium mass signals are listed in Table S6.†

With PCA analysis, we were again able to statistically differentiate between areas with high intensity of strontium signals and areas with high intensity of FA and lipid signals within the analysed area of rat fat sections (Fig. S4†).

To obtain a mass spectrum with a higher mass resolution as well as better mass accuracy, we used the OrbiTrap™ analyser (Fig. 9) of the Hybrid SIMS instrument. For imaging and

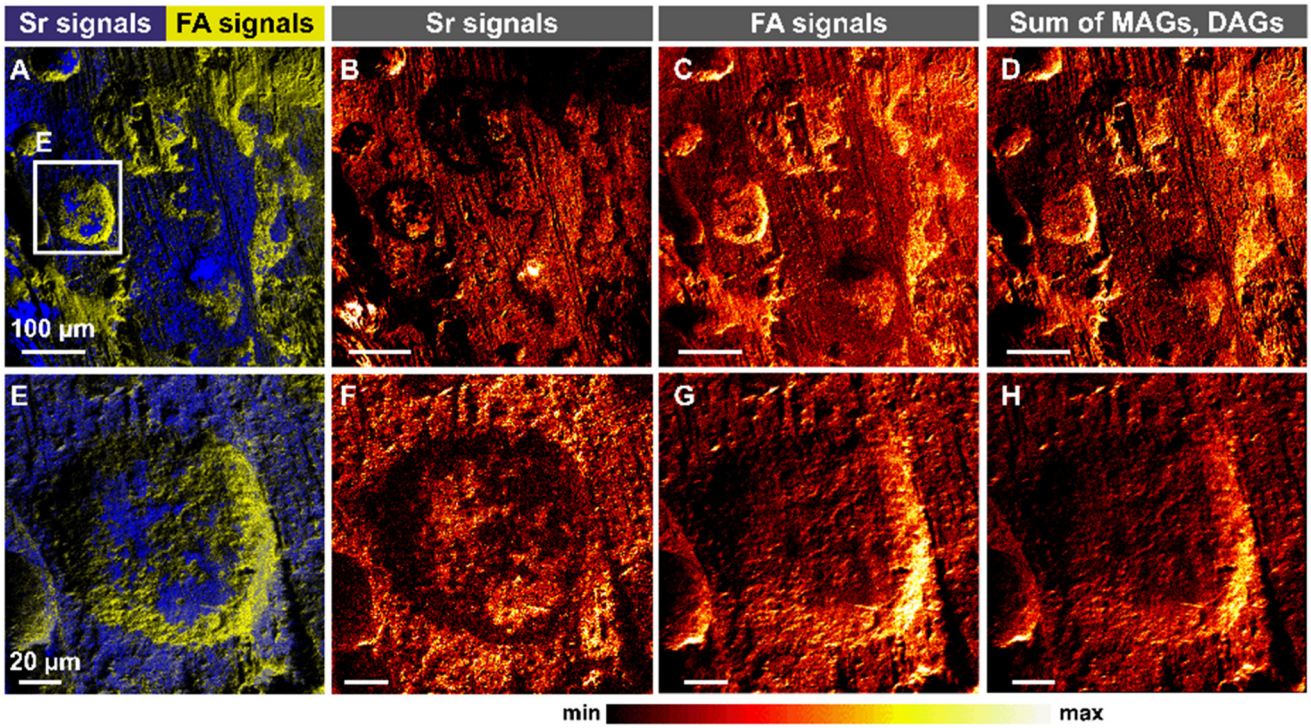

Fig. 8 2D image analysis of Sr^{2+} diffusion into a rat fat section using a Hybrid SIMS instrument in a ToF-SIMS delayed extraction mode. (A and E) In detailed, high-resolution overlay images, secondary ions originating from fatty acids (yellow) show a complementary lateral distribution as the strontium signals (blue). (B) Lateral distribution of sum of strontium mass fragments shows high intensity only in certain areas of bovine bone marrow (more detailed in F). (C) Summed signals from secondary ions originating from FA fragments (more detailed in G) and (D) from MAGs and DAGs (more detailed in H) show complementary distribution to strontium mass signals. Used mass signals for FAs, MAGs, and DAGs are listed in Table S3,† strontium mass signals are listed in Table S6.† For high-resolution imaging analysis, 30 keV Bi_3^+ cluster primary ions were applied (positive ion mode, obtained with M6 Hybrid SIMS).

spectral analysis, GCIB was used (20 keV Ar_{3000}^+ clusters) as primary ion gun instead of Bi_3^+ clusters. Two ROIs were selected of an Orbitrap image of a rat fat section, after assigning strontium and fatty acid/lipid signals (Fig. 9A). ROI 1 was in an area with high mass signal intensities of lipids/fatty acids ion species. ROI 2 was in an area with high intensities of strontium signals. The analysis of the obtained mass spectra showed a clear difference between ROI 1 and ROI 2 regarding the intensities of their mass signals (Fig. 9B). In ROI 1, mainly MAGs and DAGs (Fig. 9D and E; signals listed in Table S7†) were detectable with higher signal intensities than in the mass spectrum of ROI 2. In contrast, strontium signals could be detected with higher signal intensities in ROI 2 than in ROI 1 (Fig. 9C).

4. Discussion

Research, development, and subsequent validation of new cement materials for optimal healing of osteoporotic fractures still requires animal testing. Mathematical simulations of the release and distribution of fracture healing substances from such biomaterials into different compartments of bone could enable optimization of material development in advance of animal testing. With this approach animal testing can be reduced in future, thus following the ethical guiding principles for research and testing involving animals.[61–63] Here, our focus lies in the analysis of Sr^{2+} as active, fracture healing promoting agent, *e.g.*, as shown in the study of Thormann *et al.*[4] The osteoporotic rat as animal model has been used in a large number of studies which have investigated the positive influence of strontium on osteoporotic fracture healing in rats.[4,8,16,64–66] The diffusion of Sr^{2+} ions in cortical rat bone[21] as well as trabecular rat bone[20] were already determined in previous studies by our group. Therefore, the focus of the present study is the determination of the diffusion behavior of Sr^{2+} in rat bone marrow to subsequently perform simulations using all determined diffusion coefficients of the different bone parameters.

Due to its complex composition and non-homogenous structure, investigation of passive Sr^{2+} diffusion in bone marrow is non-trivial. In general, bone marrow exists in two different states:[38–40,67] the osteogenic state, also called red bone marrow, and the yellow bone marrow, which develops during bone maturation. While red bone marrow mostly contains haematopoietic cells (red/white blood cells, platelets)[36,38,39] as well as highly organised stroma with different cell types (*e.g.*, mesenchymal stem cells, fibroblasts,

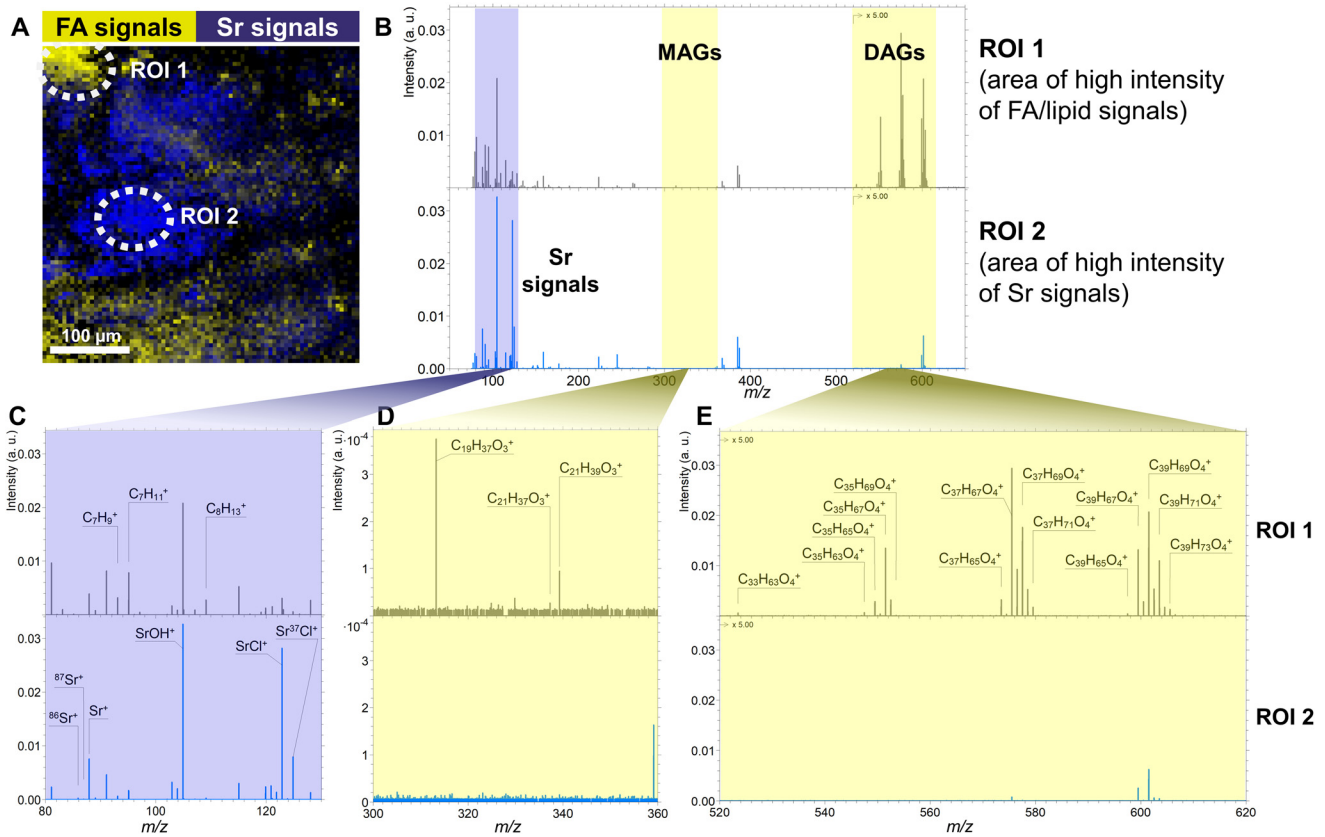

Fig. 9 3D OrbiSIMS analysis of Sr^{2+} diffusion into rat fat section using the OrbiTrap™ analyser. (A) Overlay of ion images of FA/lipid signals (yellow) and strontium signals (blue). Dotted circles show the chosen areas of ROI 1 and ROI 2, respectively. ROI 1 is in an area with high intensity of fatty acid/lipid mass signals. ROI 2 is in an area with signal high intensity of strontium species. (B) Positive mass spectra of ROI 1 and ROI 2 in a mass range of *m/z* 50–650. Mass signals from MAGs and DAGs are marked in yellow. Mass range with strontium signals is marked in blue. (C) Detailed mass range of *m/z* 80–130 shows higher intensities of strontium signals in ROI 2 than in ROI 1. (D) Detailed mass range of *m/z* 300–360 shows higher intensities of mass fragments derived from MAGs in ROI 1 than in ROI 2. (E) Detailed mass range of *m/z* 520–620 shows higher intensities of mass fragments derived from DAGs in ROI 1 than in ROI 2. For comparison of the peak intensities, the spectra were normalised to the total counts (scale spectra by total counts). Identified peaks are listed in Table S7.† For Orbitrap imaging and spectral analysis, 20 keV Ar_{3000}^{+} cluster primary ions were applied (positive ion mode, obtained with M6 Hybrid SIMS).

adipocytes, osteoblasts, osteoclasts, macrophages or endothelial cells),[36,38,39] yellow bone marrow is mainly composed of bone marrow adipocytes, with their number increases up to 70–80% during bone maturation.[38–40] Thus, bone marrow is a highly viscous, lipid-rich, and water-containing tissue, which makes the experimental determination of the diffusion of Sr^{2+} in bone marrow challenging. To our best knowledge, there are currently no methods reported in the literature for studying ion diffusion in bone marrow, except our previous study on bovine bone marrow.[41]

Nevertheless, a number of medical studies have determined the apparent diffusion coefficient (ADC) of water in bone marrow non-invasively by diffusion-weighted magnetic resonance imaging (DW-MRI).[38,68–72] It has to be noted that, although the ADC is usually given in square millimeters per second,[73] we have converted the values to square centimeters per second for better comparison (see Table S8†). Water movement in biological tissue is mainly influenced by microscopic cellular tissue structures (*e.g.*, intra- and extracellular macromolecules, cell membranes, cell organelles, fibres).[68,73] This restriction of the free self-diffusion of water molecules leads to ADC values between (2–6) × 10^{-6} cm^2 s^{-1} in normal human vertebral bone marrow.[68] In another study, Liu *et al.* determined an ADC value of about 4 × 10^{-6} cm^2 s^{-1} in bone marrow of aged osteoporotic rats, which is within the same range.[69]

For determination of Sr^{2+} diffusion in bone marrow, in a previous study of our group,[20] we made the assumption that Sr^{2+} mobility in bone marrow should be lower than both the mobility of water in bone marrow and the diffusion of Sr^{2+} in water (7.91 × 10^{-6} cm^2 s^{-1}). This is due to the double positive charge of strontium ions, which is supposed to have an attractive effect on other charged ions in the bone marrow. Overall, considering these effects of hindered mobility, a value of 1 × 10^{-8} cm^2 s^{-1} was estimated.[20] Based on this estimated value, we developed a specific cryo-ToF-SIMS depth profiling protocol for determining the relatively fast diffusion of Sr^{2+} ions into bovine bone marrow.[41] Here, experimental parameters, *e.g.*, cooling process to stop further Sr^{2+} diffusion or residence time

of Sr^{2+} solution on bone marrow, were optimised to meet the assumption that the diffusion coefficient should not be higher than 10^{-8} cm^2 s^{-1}. Indeed, we were able to determine a diffusion coefficient of $(1.93 \pm 2.40) \times 10^{-9}$ cm^2 s^{-1} for passive Sr^{2+} transport in bovine bone marrow (total measurement area, listed in Table S8†).[41] Despite some limitations of this study,[41] we could show that our passive transport model of Sr^{2+} diffusion was sufficient to successfully determine the migration rate of Sr^{2+} in different areas of bovine bone marrow. Based on these results, we have therefore applied and modified the developed cryo-ToF-SIMS protocol to the determination of the diffusion of Sr^{2+} ions in osteoporotic rat bone sections in this current study.

In the study of the passive Sr^{2+} transport in bovine bone marrow, diffusion from an exhaustless source into semi-infinite space was assumed as boundary conditions for the solution of Fick's second law of diffusion (eqn (2)).[41] Nevertheless, in the present proof-of-concept study, those boundary conditions cannot longer be assumed since residence time of $SrCl_2$ on the surface of rat bone sections had to be shortened in comparison to the experiments with bovine bone marrow. This is due to the experimentally limited thickness of rat bone sections. Thus, diffusion no longer starts from an exhaustless source, but rather with a given amount of Sr^{2+} (I_0) deposited on a certain area A of the bone marrow.[58,59] Therefore, boundary conditions for the spatial variables as well as an initial condition for time had to be redefined for this case of instantaneous plane source diffusion for determining Sr^{2+} diffusion in osteoporotic rat bone marrow.[58,60] For comparison, we plotted both diffusion fit models to the experimental obtained Sr^{2+} diffusion profiles, resulting in the better description of the diffusion process of Sr^{2+} ions in rat bone marrow by the second fit model (eqn (3), Fig. 2). For Sr^{2+} diffusion in osteoporotic rat bone marrow, an average diffusion coefficient of $D_{rat,TA}=(8.89 \pm 5.37) \times 10^{-10}$ cm^2 s^{-1} was obtained (total measurement area, Fig. 3; listed in Tables S4 and S8†). This value determined in the current study is only about one order of magnitude lower than the value estimated by our group[20] before. One possible reason for this discrepancy is discussed in detail in the following.

Same as in bovine bone marrow,[41] 2D and 3D ToF-SIMS image analysis (Fig. 3–5 and Fig. S2†) revealed that in osteoporotic rat bone marrow, there are areas of slower and areas of faster Sr^{2+}diffusion. Areas with slower Sr^{2+} diffusion could be assigned to bone marrow areas with high intensity of ion species originating from fatty acids and lipids. In contrast, areas with faster Sr^{2+} diffusion showed lower intensities of secondary ions originating from FAs/lipids. Histological staining of bone sections previously characterised with OrbiSIMS and ToF-SIMS showed good agreement between lipid species stained with Sudan Black B and the results of SIMS imaging analysis (Fig. 7). Sudan Black B binds with high affinity to lipids in the cell membrane and also to the granules in monocytes, which gives the stain a black color differentiation, while lipid droplets are stained dark purple. The spatial distribution of the detected ion fragments of lipids/FAs are in agreement with the histological staining of lipid-rich bone marrow areas. It should be noted, however, that by means of ToF-SIMS the distinction between FA/lipid fragments originating from cell membranes and FA/lipid fragments originating from lipid droplets is hardly possible. Nevertheless, signal intensities of strontium ion species were indeed lower in areas that were stained intensively with Sudan Black B and higher in areas, which were not stained with Sudan Black B. This means that cell structures within bone marrow (*e.g.*, cell membranes, adipocytes) with high amount of FAs and lipids prevent diffusion of Sr^{2+} ions. With additional ToF-SIMS imaging analyses of Sr^{2+} diffusion into pure fat sections from rats (Fig. 8 and Fig. S3†) as well as OrbiSIMS spectral analyses (Fig. 6 and 9), we could confirm these observations, which are also in line with our results from studying Sr^{2+} diffusion in bovine bone marrow.[41] Yeung *et al.* showed that a decrease in ADC values is correlated with an increasing amount of fat cells in bone marrow.[74] The diffusion of water thus becomes less with an increasing proportion of fat cells in the bone marrow. These results were also found by Nonomura *et al.*[70] Hence, these studies show that the accumulation of fat cells in bone marrow may reduce extracellular diffusion. The results of our study also show slower Sr^{2+} diffusion in areas with high signal intensity at fatty acid/lipid ion fragments. Thus, our findings are in line with literature, suggesting that not only the diffusion of water in bone marrow may be reduced because of accumulation of fat cells, but also the diffusion of Sr^{2+} ions. This possible lipid induced reduction of Sr^{2+} diffusion in bone marrow was not considered in the theoretical estimation of the Sr^{2+} diffusion coefficient.[20] Because knowledge of this phenomenon was not yet available at the time of this early study, as a result, the diffusion coefficient was probably estimated to be higher than it actually is. This demonstrates the important significance of the current study in which we demonstrated inhibition of strontium diffusion in rat bone marrow by lipid and fatty acid species.

Nevertheless, an important limitation when comparing our experimentally determined values for Sr^{2+} diffusion in rat bone marrow with the estimated value[20] as well as values found in the literature for water diffusion in bone marrow (Table S8†) are the respective diffusion models. While ADC values are based on the assumption of self-diffusion of water, which is restricted by the microscopic cellular tissue structure,[68] in this study, we applied a biologically passive diffusion model of chemical diffusion based on a concentration gradient. In addition, we determined Sr^{2+} diffusion on biologically inactive *ex vivo* samples, disregarding the involvement of active cells and mass transport *via* the vascular system of the bone marrow. However, an analytical *in vivo* determination of the active Sr^{2+} mobility in bone marrow *via* its vascular system is methodologically difficult to implement.[41] MRI is one of the few possibilities to determine the spatial drug distribution *in vivo*, as shown *e.g.* by Giers *et al.*[75] In their study, the distribution of a marker could be observed after its release from an implanted bone cement. Nonetheless, it was not possible to observe the active substance itself, but only the marker.[75] Furthermore, a high drug concentration was necessary for the MRI studies, and they had to be carried out within a few hours after implantation, as the drug concentration drops rapidly

due to dispersion into the environment.[75] Therefore, post-mortem studies using analytical methods for imaging and estimating drug distribution in the bone marrow, as we have done here with cryo-ToF-SIMS and cryo-OrbiSIMS, are an experimentally feasible alternative.

In addition, it has to be noted that a limitation of our diffusion model is the simplified determination of the diffusion coefficient. Although our study suggests that FAs and lipids prevent Sr^{2+} ion diffusion, we calculated an overall diffusion coefficient for this first model approach, including all different bone marrow cell types and structures. For future studies, a more advanced model must be refined for more precise diffusion coefficients considering different cell components of the bone marrow. However, aim of this paper was to present a first approach to experimentally investigate strontium diffusion in spatially intact rat bone marrow sections. For this purpose, the diffusion coefficient of strontium diffusion throughout the total bone marrow area is best suited.

For OrbiSIMS analysis, GCIB was used as primary ion gun instead of LMIG. Although Bi_3^+ clusters as primary ions provide mass images with higher lateral resolution with ToF mass analysers, the disadvantage of Bi_3^+ clusters is the high fragmentation of biomolecules (*e.g.*, lipid and fatty acid species). Since we were interested in mass spectra richer in intact lipids, we applied GCIB as primary ion beam with Ar_{3000}^+ as primary ion species. Ar_{3000}^+ clusters create mass spectra with significantly less fragmentation compared with LMIG primary ion beam. In addition, the primary ion current with Bi_3^+ clusters is not sufficient to produce high contrast images with OrbiTrap™ analyser. For comparison of mass accuracy between the OrbiTrap™ and the ToF analyser (ToF-SIMS measurement from Fig. 8), deviations of the assigned masses from the theoretical masses are listed in Table S7.† Especially for the inorganic strontium peaks, a better mass accuracy could be achieved with the Orbitrap analyser. Deviations obtained with the Orbitrap analyser were for most selected peaks <2 ppm, which demonstrates its unambiguous peak identification ability. In comparison, deviation obtained with the ToF analyser was >45 ppm for inorganic strontium species and >20 ppm for lipid peaks on average. Mass resolution of signals obtained with OrbiTrap™ analyser was also higher than mass resolution obtained with the ToF analyser. For inorganic strontium species, mass resolutions >100 000 could be obtained with OrbiTrap™ analyser (>2000 up to >4000 with ToF analyser). For MAGs and DAGs, mass resolutions from >40 000 up to >50 000 were achieved (ToF-analyser: >5000). Overall, this study demonstrates that OrbiSIMS analysis is beneficial for investigation of ion mobility in biological material if one is interested in mass spectra with high mass accuracy as well as mass resolution.

5. Conclusion

In conclusion, within our study we could successfully establish 2D and 3D cryo-ToF-SIMS and cryo-OrbiSIMS imaging and spectral analysis for the characterisation of Sr^{2+} mobility in the bone marrow of osteoporotic rats as well as in rat fat sections. With the diffusion coefficients of Sr^{2+} previously determined in the mineralised areas of femoral rat bone, a mathematical 3D model could now be developed and calculated in order to simulate the transport and release of Sr^{2+} from implant biomaterials into bone. Such a mathematical 3D model could help to reduce animal testing in the future since typically, after successful *in vitro* experiments, biomaterials with different Sr^{2+} fractions are tested in different animal groups to identify the optimal dose of Sr^{2+} for osteoporotic bone healing.[8] In contrast, a mathematical simulation of Sr^{2+} diffusion in bone based on the determined diffusion coefficients can help to identify the most promising biomaterial in advance to *in vivo* experiments. In this way, it is possible to define the optimal Sr^{2+} concentration in the implant material in advance, avoiding multiple animal testing groups.

Author contributions

Christine Kern performed: conceptualization, methodology, formal analysis, investigation, writing–original draft, visualization. Reem Jamous performed: investigation, visualization. Thaqif El Khassawna performed: resources, writing–review & editing. Marcus Rohnke performed: conceptualization, resources, writing–review & editing, supervision. All authors proofread the manuscript and approved the final version.

Conflicts of interest

There are no conflicts to declare.

Acknowledgements

This work was funded by the German Research Foundation (DFG, Collaborative Research Centre Transregio 79 – subprojects M5 and T1). We gratefully acknowledge the financial support within this project. MR thanks the DFG for funding of the Hybrid-SIMS (M6 Hybrid SIMS, IONTOF GmbH, Muenster, Germany) under grant number INST 162/544-1 FUGG. The authors thank Dr Stefanie Kern, Dr Felix Walther, and Dr Adrian Schürmann for many helpful discussions. All authors state that they have no conflicts of interest.

References

1 T. D. Rachner, S. Khosla and L. C. Hofbauer, *Lancet*, 2011, **377**, 1276–1287.
2 R. Eastell, T. W. O'Neill, L. C. Hofbauer, B. Langdahl, I. R. Reid, D. T. Gold and S. R. Cummings, *Nat. Rev. Dis. Primers*, 2016, **2**, 16069.
3 N. Takahashi, T. Sasaki, Y. Tsouderos and T. Suda, *J. Bone Miner. Res.*, 2003, **18**, 1082–1087.

4 U. Thormann, S. Ray, U. Sommer, T. Elkhassawna, T. Rehling, M. Hundgeburth, A. Henss, M. Rohnke, J. Janek, K. S. Lips, C. Heiss, G. Schlewitz, G. Szalay, M. Schumacher, M. Gelinsky, R. Schnettler and V. Alt, *Biomaterials*, 2013, **34**, 8589–8598.
5 P. J. Marie, P. Ammann, G. Boivin and C. Rey, *Calcif. Tissue Int.*, 2014, **69**, 121–129.
6 J. Kokesch-Himmelreich, M. Schumacher, M. Rohnke, M. Gelinsky and J. Janek, *Biointerphases*, 2013, **8**, 17.
7 D. Li, K. Chen, L. Duan, T. Fu, J. Li, Z. Mu, S. Wang, Q. Zou, L. Chen, Y. Feng, Y. Li, H. Zhang, H. Wang, T. Chen and P. Ji, *ACS Biomater. Sci. Eng.*, 2019, **5**, 1440–1451.
8 B. Kruppke, S. Ray, V. Alt, M. Rohnke, C. Kern, M. Kampschulte, C. Heinemann, M. Budak, J. Adam, N. Dohner, L. Franz-Forsthoffer, T. El Khassawna, C. Heiss, T. Hanke and U. Thormann, *Molecules*, 2020, **25**, 5103.
9 J. Zarins, M. Pilmane, E. Sidhoma, I. Salma and J. Locs, *Symmetry*, 2019, **11**, 229.
10 M. Schumacher, A. S. Wagner, J. Kokesch-Himmelreich, A. Bernhardt, M. Rohnke, S. Wenisch and M. Gelinsky, *Acta Biomater.*, 2016, **37**, 184–194.
11 S. Chandran, S. S. Babu, H. K. Vs, H. K. Varma and A. John, *J. Biomater. Appl.*, 2016, **31**, 499–509.
12 L. Maimoun, T. C. Brennan, I. Badoud, V. Dubois-Ferriere, R. Rizzoli and P. Ammann, *Bone*, 2010, **46**, 1436–1441.
13 S. G. Dahl, P. Allain, P. J. Marie, Y. Mauras, G. Boivin, P. Ammann, Y. Tsouderos, P. D. Delmas and C. Christiansen, *Bone*, 2001, **28**, 446–453.
14 M. Schumacher, A. Henss, M. Rohnke and M. Gelinsky, *Acta Biomater.*, 2013, **9**, 7536–7544.
15 A. S. Wagner, M. Schumacher, M. Rohnke, K. Glenske, M. Gelinsky, S. Arnhold, S. Mazurek and S. Wenisch, *Biomed. Mater.*, 2019, **14**, 025004.
16 V. Alt, U. Thormann, S. Ray, D. Zahner, L. Durselen, K. Lips, T. El Khassawna, C. Heiss, A. Riedrich, G. Schlewitz, A. Ignatius, M. Kampschulte, H. von Dewitz, S. Heinemann, R. Schnettler and A. Langheinrich, *Acta Biomater.*, 2013, **9**, 7035–7042.
17 O. Z. Andersen, V. Offermanns, M. Sillassen, K. P. Almtoft, I. H. Andersen, S. Sorensen, C. S. Jeppesen, D. C. Kraft, J. Bottiger, M. Rasse, F. Kloss and M. Foss, *Biomaterials*, 2013, **34**, 5883–5890.
18 Y. Li, X. Li, G. Song, K. Chen, G. Yin and J. Hu, *Clin. Oral Implants Res.*, 2012, **23**, 1038–1044.
19 W. Querido, M. Farina and K. Anselme, *Biomatter*, 2015, **5**, e1027847.
20 M. Rohnke, S. Pfitzenreuter, B. Mogwitz, A. Henß, J. Thomas, D. Bieberstein, T. Gemming, S. K. Otto, S. Ray, M. Schumacher, M. Gelinsky and V. Alt, *J. Controlled Release*, 2017, **262**, 159–169.
21 C. Kern, M. Quade, S. Ray, J. Thomas, M. Schumacher, T. Gemming, M. Gelinsky, V. Alt and M. Rohnke, *J. R. Soc., Interface*, 2019, **16**, 20180638.
22 J. S. Fletcher and J. C. Vickerman, *Anal. Chem.*, 2013, **85**, 610–639.
23 S. Ray, U. Thormann, M. Eichelroth, M. Budak, C. Biehl, M. Rupp, U. Sommer, T. El Khassawna, F. I. Alagboso, M. Kampschulte, M. Rohnke, A. Henß, K. Peppler, V. Linke, P. Quadbeck, A. Voigt, F. Stenger, D. Karl, R. Schnettler, C. Heiss, K. S. Lips and V. Alt, *Biomaterials*, 2018, **157**, 1–16.
24 C. Kern, S. Ray, M. Gelinsky, A. T. Bellew, A. Pirkl and M. Rohnke, *Biointerphases*, 2020, **15**, 031005.
25 G. X. Ni, W. W. Lu, B. Xu, K. Y. Chiu, C. Yang, Z. Y. Li, W. M. Lam and K. D. Luk, *Biomaterials*, 2006, **27**, 5127–5133.
26 C. Eriksson, P. Malmberg and H. Nygren, *Rapid Commun. Mass Spectrom.*, 2008, **22**, 943–949.
27 A. Palmquist, L. Emanuelsson and P. Sjövall, *Appl. Surf. Sci.*, 2012, **258**, 6485–6494.
28 M. Rohnke, A. Henss, J. Kokesch-Himmelreich, M. Schumacher, S. Ray, V. Alt, M. Gelinsky and J. Janek, *Anal. Bioanal. Chem.*, 2013, **405**, 8769–8780.
29 K. Schaepe, J. Werner, K. Glenske, T. Bartges, A. Henss, M. Rohnke, S. Wenisch and J. Janek, *Anal. Bioanal. Chem.*, 2017, **409**, 4425–4435.
30 P. Malmberg, U. Bexell, C. Eriksson, H. Nygren and K. Richter, *Rapid Commun. Mass Spectrom.*, 2007, **21**, 745–749.
31 P. Malmberg and H. Nygren, *Proteomics*, 2008, **8**, 3755–3762.
32 A. Henss, M. Rohnke, S. Knaack, M. Kleine-Boymann, T. Leichtweiss, P. Schmitz, T. El Khassawna, M. Gelinsky, C. Heiss and J. Janek, *Biointerphases*, 2013, **8**, 31.
33 S. A. Elmore, *Toxicol. Pathol.*, 2006, **34**, 666–686.
34 G. S. Travlos, *Toxicol. Pathol.*, 2006, **34**, 566–598.
35 G. S. Travlos, *Toxicol. Pathol.*, 2006, **34**, 548–565.
36 U. A. Gurkan and O. Akkus, *Ann. Biomed. Eng.*, 2008, **36**, 1978–1991.
37 A. Birbrair and P. S. Frenette, *Ann. N. Y. Acad. Sci.*, 2016, **1370**, 82–96.
38 B. C. Vande Berg, J. Malghem, F. E. Lecouvet and B. Maldague, *Eur. Radiol.*, 1998, **8**, 1327–1334.
39 E. V. Morris and C. M. Edwards, *Front. Endocrinol.*, 2016, **7**, 90.
40 D. C. Karampinos, S. Ruschke, M. Dieckmeyer, M. Diefenbach, D. Franz, A. S. Gersing, R. Krug and T. Baum, *J. Magn. Reson. Imaging*, 2018, **47**, 332–353.
41 C. Kern, A. Pauli and M. Rohnke, *Rapid Commun. Mass Spectrom.*, 2022, **n/a**, e9300.
42 A. Raic, T. Naolou, A. Mohra, C. Chatterjee and C. Lee-Thedieck, *MRS Commun.*, 2019, **9**, 37–52.
43 M. H. Abd-El-Aal and M. S. Mohamed, *Food Chem.*, 1989, **31**, 93–103.
44 S. K. Das, M. T. Scott and P. K. Adhikary, *Lipids*, 1975, **10**, 584–590.
45 A. M. Pino and J. P. Rodriguez, *Bone*, 2019, **118**, 53–61.
46 F. C. Mello Jr., R. A. Field, S. Forenza and J. E. Kunsman, *J. Food Sci.*, 1976, **41**, 226–230.
47 J. Paccou, G. Penel, C. Chauveau, B. Cortet and P. Hardouin, *Bone*, 2019, **118**, 8–15.

48 A. During, G. Penel and P. Hardouin, *Prog. Lipid Res.*, 2015, **59**, 126–146.
49 B. Y. Lau, V. A. Fajardo, L. McMeekin, S. M. Sacco, W. E. Ward, B. D. Roy, S. J. Peters and P. J. Leblanc, *Appl. Physiol. Nutr. Metab.*, 2010, **35**, 598–606.
50 E. Mulder, J. De Gier and L. L. M. Van Deenen, *Biochim. Biophys. Acta*, 1962, **59**, 502–504.
51 G. J. Miller, M. R. Frey, J. E. Kunsman and R. A. Field, *J. Food Sci.*, 1982, **47**, 657–660.
52 M. WAJDA, *Biochem. J.*, 1965, **95**, 252–255.
53 M. Passarelli, A. Pirkl, R. Moellers, *et al.*, *Nat. Methods*, 2017, **14**, 1175–1183.
54 K. Schaepe, D. R. Bhandari, J. Werner, A. Henss, A. Pirkl, M. Kleine-Boymann, M. Rohnke, S. Wenisch, E. Neumann, J. Janek and B. Spengler, *Anal. Chem.*, 2018, **90**, 8856–8864.
55 F. Davey and D. Nelson, B. Sudan Black, In *Hematology*, ed. W. J. Williams, E. Beutler, A. J. Erslev, R. W. Rundles, McGraw-Hill, New York, 2nd edn, 1977, pp. 1629–1630.
56 D. Malhan, M. Muelke, S. Rosch, A. B. Schaefer, F. Merboth, D. Weisweiler, C. Heiss, I. Arganda-Carreras and T. El Khassawna, *Front. Endocrinol.*, 2018, **9**, 666.
57 T. Stephan, *Planet. Space Sci.*, 2001, **49**, 859–906.
58 P. W. Atkins, J. de Paula, M. Bär, A. Schleitzer and C. Heinisch, *Physikalische Chemie*, Wiley, 2006.
59 J. Crank, *The mathematics of diffusion*, ed. J. Crank, Clarendon Press, Oxford [England], 1975.
60 M. A. Climent, G. de Vera, J. F. López, E. Viqueira and C. Andrade, *Cem. Concr. Res.*, 2002, **32**, 1113–1123.
61 P. Flecknell, *Altex*, 2002, **19**, 73–78.
62 L. U. Sneddon, L. G. Halsey and N. R. Bury, *J. Exp. Biol.*, 2017, **220**, 3007–3016.
63 H. Wurbel, *Lab. Anim.*, 2017, **46**, 164–166.
64 K. E. Ozturan, B. Demir, I. Yucel, H. Cakıcı, F. Yilmaz and A. Haberal, *J. Orthop. Res.*, 2011, **29**, 138–142.
65 N. Mardas, X. Dereka, A. Stavropoulos, M. Patel and N. Donos, *J. Periodontal Res.*, 2021, **56**, 330–338.
66 M. R. Katunar, J. I. Pastore, A. Cisilino, J. Merlo, L. Salemme Alonso, M. Baca, K. Haddad, S. Cere and J. Ballarre, *Surf. Coat. Technol.*, 2022, **433**, 128159.
67 E. Zhao, H. Xu, L. Wang, I. Kryczek, K. Wu, Y. Hu, G. Wang and W. Zou, *Cell. Mol. Immunol.*, 2012, **9**, 11–19.
68 O. Dietrich, T. Geith, M. F. Reiser and A. Baur-Melnyk, *NMR Biomed.*, 2017, **30**, e3333.
69 Y. Liu, L. Cao, J. Hillengass, S. Delorme, G. Schlewitz, P. Govindarajan, R. Schnettler, C. Heiss and T. Bauerle, *Acta Radiol.*, 2013, **54**, 205–213.
70 Y. Nonomura, M. Yasumoto, R. Yoshimura, K. Haraguchi, S. Ito, T. Akashi and I. Ohashi, *J. Magn. Reson. Imaging*, 2001, **13**, 757–760.
71 J. Hillengass, B. Stieltjes, T. Bauerle, F. McClanahan, C. Heiss, T. Hielscher, B. Wagner-Gund, V. Habetler, H. Goldschmidt, H. P. Schlemmer, S. Delorme and C. M. Zechmann, *Acta Radiol.*, 2011, **52**, 324–330.
72 J. R. Reichenbach, *Rofo*, 2013, **185**, RK402_402.
73 A. R. Padhani, D.-M. Koh and D. J. Collins, *Radiology*, 2011, **261**, 700–718.
74 D. K. Yeung, S. Y. Wong, J. F. Griffith and E. M. Lau, *J. Magn. Reson. Imaging*, 2004, **19**, 222–228.
75 M. B. Giers, A. C. McLaren, K. J. Schmidt, M. R. Caplan and R. McLemore, *J. Biomed. Mater. Res., Part B*, 2014, **102**, 806–814.